ORCA – Online Research @ Cardiff

Journal Pre-proof

Drivers for mass and momentum exchange between the main channel and river bank lateral cavities

Pablo Ouro, Carmelo Juez, Mário Franca

Please cite this article as: Pablo Ouro, Carmelo Juez, Mário Franca, Drivers for mass and momentum exchange between the main channel and river bank lateral cavities, *Advances in Water Resources* (2020), doi: https://doi.org/10.1016/j.advwatres.2020.103511

This is a PDF file of an article that has undergone enhancements after acceptance, such as the addition of a cover page and metadata, and formatting for readability, but it is not yet the definitive version of record. This version will undergo additional copyediting, typesetting and review before it is published in its final form, but we are providing this version to give early visibility of the article. Please note that, during the production process, errors may be discovered which could affect the content, and all legal disclaimers that apply to the journal pertain.

Highlights

- Pressure gradient is the main responsible for the cavity momentum flush-out.

- Sediment deposition pathways coincide with regions of low turbulent kinetic energy.

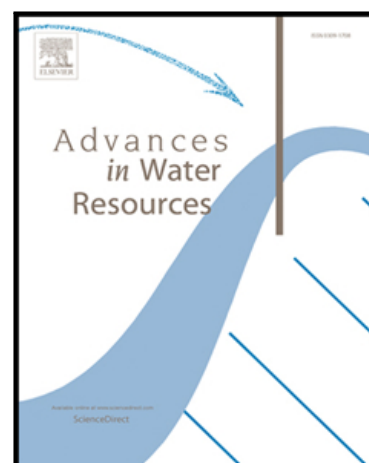- Kelvin-Helmholtz vortices generated in the cavity shear layer prevent mass exchange.

Drivers for mass and momentum exchange between the main channel and river bank lateral cavities

Pablo Ouro[a,*], Carmelo Juez[b], Mário Franca[c,d]

[a]*Hydro-environmental Research Centre, School of Engineering, Cardiff University. The Parade CF24 3AA, Cardiff, United Kingdom.*
[b]*Instituto Pirenaico de Ecología, Consejo Superior de Investigaciones Científicas (IPE-CSIC), Campus de Aula Dei, Avenida Montañana 1005, 50059 Zaragoza, Spain.*
[c]*IHE-Delft Institute for Water Education, Delft, The Netherlands.*
[d]*Department of Hydraulic Engineering, Delft University of Technology, Delft, The Netherlands.*

Abstract

Large-Eddy Simulations (LES) are used to investigate the governing processes involved in mass and momentum transfer between the flow in the main channel and symmetrically-distributed lateral bank cavities. In-cavity free-surface velocities, based on laboratory measurements made in an open channel, are used to validate the numerical results. A main vortical structure dominates the in-cavity flow which, despite the shallow nature of the flow, features a remarked three dimensional dynamics. LES results outline the largest velocities through the mouth of the cavity are attained in two thin regions near the bottom-bed and free-surface. In the shear layers established between the main channel and cavities is where the main transfer of turbulent momentum is made between these two flow regions, and the numerical simulations capture well the instantaneous coherent flow structures, e.g. Kelvin-Helmholtz vortices. LES captures a low-frequency standing wave phenomenon even with a rigid-lid approximation adopted at the free-surface boundary. Momentum exchange between cavities and main channel is analysed using the Reynolds Averaged momentum equation in the transverse direction, revealing that the pressure gradient term is the unique contributor to flushing momentum out of the cavities whilst convection and Reynolds

---

*Corresponding author
Email addresses: `ourop@cardiff.ac.uk` (Pablo Ouro), `carmelo.juez@ipe.csic.es` (Carmelo Juez), `m.franca@un-ihe.org` (Mário Franca)

normal stress terms are responsible for its entraining into the cavity. Furthermore, sediment deposition areas documented in the laboratory experiments are linked with the simulated hydrodynamics, which correlate with regions of low turbulent kinetic energy and vertical velocities near the bottom of the channel. Overall, the results shed new light into the complex mechanisms involved in mass and momentum transfer; this will aid to design embayments more efficiently regarding sediment transport processes.

1. Introduction

Lateral embayments or cavities are often present in natural or human-influenced rivers. In natural rivers these typically constitute areas of sediment accumulation and flow velocity diversity, making these areas ecology hotspots within the fluvial network and controls of the river basin distribution of water and sediments. Artificial lateral cavities or local widening are often implemented in channelised rivers as nature-inspired river restoration measures. Anthropologically altered rivers have typically uniform cross sections and monotonous river banks, which contrast with natural river channels where large-scale and diversified flow and morphology can be found. This hinders the development of fish and vegetation habitats that require areas with differentiated flow velocities (Wood and Armitage [1], Kemp et al. [2]). With the intention to foster new flow patterns that diversify the velocity fields and promote the accumulation of sediment and sheltering conditions for aquatic biota, local widening establishing lateral embayments or cavities is a common practice in restoration projects mimicking natural conditions. The so-called Wandos in Japan are built to enable areas for fish spawning and nursery (Uno et al. [3], Nezu and Onitsuka [4]) and Ribi et al. [5] showed the suitability of lateral embayments to provide shelter to fish. Harbors in rivers may be conceptualised as cavities lateral to the flow in the main channel, and these may be subjected to siltation of material transported in the main stream (Langendoen et al. [6], van Schijndel and Kranenburg [7]). Finally, lateral embayments may be artificially created to capture fine sediments and thus maintain a central navigable channel, as in the historical case of the *casiers de Girardon* in the lower-Rhône (France) (Thorel et al. [8]).

A thorough design of the geometry of such local widenings in a river reach

3

27 is needed in terms of their impact on the channel hydrodynamics (Valentine
28 and Wood [9], Uijttewaal et al. [10], Weitbrecht et al. [11], Lesack and Marsh
29 [12], Sukhodolov [13], Akutina [14], Mignot et al. [15], Navas-Montilla et al.
30 [16]) and on the transport of such environmental variables as fine sediments
31 (Juez et al. [17, 18]), pollutants, oxygen and nutrients (Jackson et al. [19,
32 20], Sanjou et al. [21]). As a result, numerous field, laboratory and numerical
33 studies were carried out to elucidate the mass and momentum exchange
34 mechanisms between the main flow and the lateral cavities.

35 Traditionally, it has been common to derive mass and momentum fluxes
36 from the flow patterns observed on the water surface of laboratory experi-
37 ments and in the field. However, this approach based on the superficial flow
38 features over-simplifies the complexity of these flows and ignore the possible
39 three-dimensional (3D) nature of the exchange processes observed in the in-
40 teraction between the main flow and lateral embayments. Conceived from the
41 existing knowledge in the literature, Figure 1 presents a conceptual model of
42 open-channel flow when lateral embayments perpendicular to the main flow
43 are present, which includes: a main recirculating vortex inside the cavity
44 occupying most of its volume; vertically-oriented coherent structures which
45 are shed from the shear layer with a frequency f_{SL}; secondary low-energetic
46 vortices in the internal corners of the cavity; and standing resonant waves
47 that appear due to the enclosed water domain (also called seiches, Kimura
48 and Hosoda [22]) oscillating at a frequency f_{SW} in the cross-flow direction
49 and causing important pressure fluctuations.

50 Transport and settling of sediments in open channel flow can vary de-
51 pending on the flow conditions, cross-section, channel aspect ratio or physical
52 properties of the sediments, among others. Nikora and Goring [23] evidenced
53 that turbulence is a key factor in sediment transport flux, which is often ne-
54 glected and sediment flux is often associated solely to the mean flow, and
55 that phenomena such as turbulent bursting events are well correlated in time
56 with sediment transport processes. A larger degree of complexity arises in
57 curved channels or when lateral embayments perpendicular to the main flow
58 are found.

59 Juez et al. [17] carried out systematic laboratory experiments in an open
60 channel, with a large number of different geometries of lateral embayments in
61 the channel banks, to investigate the interplay between flow hydrodynamics
62 and the transport (under suspension) and accumulation of fine sediments.
63 The in-cavity sedimentation pattern for several combinations of geometrical
64 configurations and flow conditions were analysed under a two-dimensional
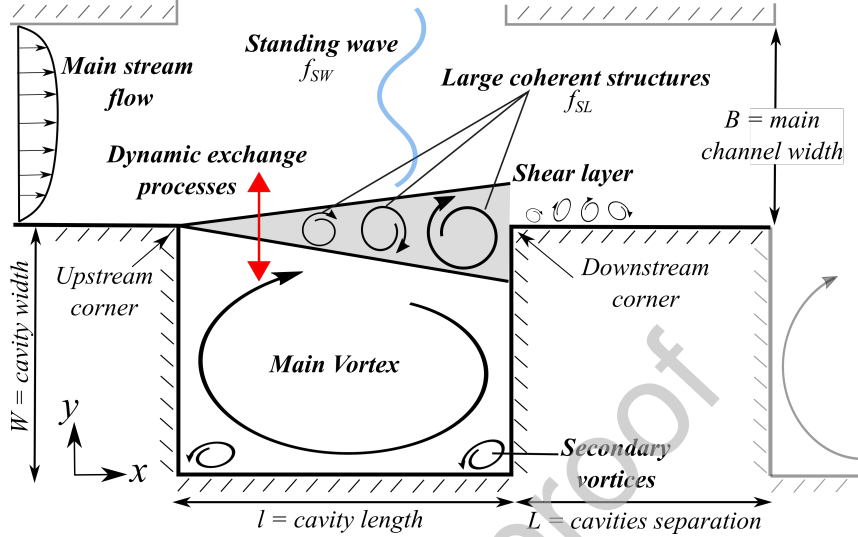
4

Figure 1: Schematic of the flow phenomena typically present in the hydrodynamics of lateral bank cavities. The lateral cavities are characterised by the cavity length l, the distance between two cavities L and the lateral width of the cavities W.

framework. However, the results pointed out the existence of 3D flow features which relate the location and magnitude of the in-cavity flow patterns with sedimentation patterns and amount of fine sediment trapped. In their studies, Juez et al. [17, 24] observed evidences that the three-dimensionality of the flow was non-negligible, especially for the less shallow flow conditions, which did not allow to fully elucidate the direct link between the flow and the sediment transport processes.

To unravel the details of such complex flow, high-fidelity detailed numerical simulation tools were used. Both Detached-Eddy Simulations (DES) and Large-Eddy Simulations (LES) are techniques that aid to understand the hydrodynamics of multi-scale turbulent flow structures under the presence of groynes and lateral embayments (McCoy et al. [25], Constantinescu et al. [26], Fang et al. [27]). These computational approaches, if equipped with the necessary high spatial resolution, can accurately resolve the dominant quasi-2D flow structures, e.g. large-scale energetic or shear-layer vortices, and also smaller 3D vortices. DES or LES not just provide the required resolution of the turbulent structures but they can accurately predict areas of flow separation of high importance in open channel and river flows, proving their superiority to Reynolds Averaged Navier-Stokes (RANS) computations (van

5

84 Balen et al. [28], Juez et al. [29], Navas-Montilla and Murillo [30]). Thus,
85 these eddy-resolving techniques provide valuable and complete information
86 of the turbulent flow dynamics (Ouro et al. [31]), which ultimately, govern
87 mass and momentum exchange processes (McCoy et al. [32], Gualtieri [33]).
88 This paper conducted numerical simulations by means of LES to reveal
89 3D flow hydrodynamics (i.e. mass/momentum fluxes and turbulent struc-
90 ture) in lateral embayments of open-channel flows. The numerical results
91 contribute to determine the underlying physical mechanisms for mass and
92 momentum transfer between the main channel and the lateral embayments
93 as well as also evidencing about the feasibility of considering the flow shal-
94 lowness (2D). Ultimately, these outcomes are related to the sediment ero-
95 sion/transport processes observed in the laboratory experiments by Juez
96 et al. [24]. Furthermore, the identification of preferential regions for mass and
97 momentum transfer across the opening of the cavities is possible through the
98 results of the numerical simulations. This is essential information in what
99 concerns the design of lateral embayments either to function as river restora-
100 tion measures, as fluvial harbours or as sediment traps to keep main channels
101 navigable. The present study focuses on one geometrical configuration ex-
102 perimentally tested in Juez et al. [17] with three different flow discharges.
103 This geometrical configuration was chosen from others previously investi-
104 gated, since it corresponded to sedimentation patterns which contained flow
105 diversity and morphology, hence ideal as nature-inspired solution for river
106 restoration. The numerical simulations herein outlined adopt the large-eddy
107 simulation approach to resolve the governing equations using the in-house
108 code Hydro3D (Ouro et al. [34]). Despite these large-eddy simulations do
109 not consider the sediment transport, the hydrodynamic results serve as a
110 proxy to link the flow fluxes to the observed sediment transport pathways.

2. Laboratory experiments and numerical simulations

2.1. Laboratory setup

113 Experiments were carried out in a channel which works in a closed circuit
114 with the following components (see Juez et al. [17, 18] for a more detailed
115 description): (i) an upstream 2 m long, 1 m wide and 1 m high tank for
116 mixing suspended sediments, (ii) a rectangular 7.5 m long, 1.0 m wide and
117 1.0 m high open-channel with 0.1% slope, and (iii) a downstream tank of 3.5
118 m long, 1 m wide and 1 m high that collects the water and sediments for
119 recirculation. The water is pumped from the downstream to the upstream

6

120 tank through a pipe system equipped with a valve to control the discharge
121 and a flow meter. The channel bottom is smooth and made of painted wood.
122 Upstream, the transition between the head tank and the channel reach is
123 made by a honeycomb-type flow tranquilliser. Downstream from the channel,
124 a Venetian gate allows the flow depth to be controlled. The base channel
125 banks were modified by placing concrete bricks by the lateral walls. This
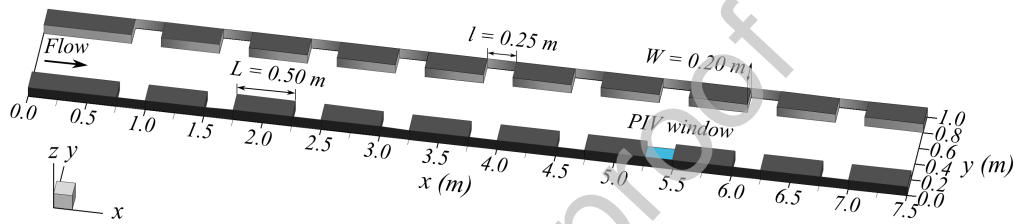126 allowed to build lateral embayments in the laboratory channel (see Figure
127 2).

Figure 2: Representation of the channel configuration tested in Juez et al. [17], including the relevant geometric dimensions. The cavity in which PIV measurements were taken is highlighted in blue.

128 Two-dimensional (2D) surface velocity fields in the lateral embayments
129 were measured by means of surface PIV technique. Therefore, instantaneous
130 (u, v), mean (U, V) and fluctuating (u', v') values for the streamwise and
131 spanwise velocities were recorded at the water surface. The water level was
132 recorded all through the experiments by an ultrasonic probe.

133 Uniform fine sediment with a $d_{50} = 0.2$ mm was supplied in the upstream
134 tank of the channel at the beginning of each test. The mean diameter of the
135 fine sediment particles was representative of the Rhône river (Federal Office
136 of Environment [35]). Sediments were trapped inside the lateral cavities.
137 At the end of the experiments, the sediment deposits inside the cavities
138 were photographed. The obtained photos were treated to determine the area
139 occupied by the settled sediments.

140 The lateral embayments configuration studied in this work corresponds to
141 geometrical configuration 2.1 in Juez et al. [17], i.e. 0.25 m long (l) and 0.20 m
142 wide (W) cavities with a streamwise spacing between consecutive cavities (L)
143 of 0.40 m. The main channel width (B) is 0.60 m. Three different discharges
144 were tested experimentally, which correspond to different values of the ratio
145 between the water height, h, and the channel width, b: $b/h = 17.26$ - 7.20;
146 i.e. from more to less shallow uniform flow conditions. Table 1 displays

7

147 the main flow characteristics of the experiments herein studied, namely flow
148 discharge (Q), water depth (h), bulk velocity (U_0), bulk Reynolds number
149 ($Re = hU_0/\nu$, where ν is the water kinematic viscosity), and Froude number
150 ($Fr = U_0/(gh)^{1/2}$, where g stands for the gravity acceleration).

Case	Q	h	U_0	Re	Fr
	[L/s]	[m]	[m/s]	[-]	[-]
Q1	4.8	0.035	0.227	28,487	0.39
Q2	8.5	0.050	0.295	50,568	0.42
Q3	15.0	0.070	0.355	80,645	0.43

Table 1: Hydrodynamic conditions of the configurations studied.

151 *2.2. Numerical framework*

152   High-fidelity numerical simulations are performed using the in-house code
153 Hydro3D (Ouro et al. [36]), which resolves the flow dynamics by means of
154 Large-Eddy Simulation (LES) (Liu et al. [37], Ouro et al. [31, 38], Stoesser
155 [39], Stoesser et al. [40]). In the framework of LES, the flow structures
156 larger than a given filter size, e.g. grid spacing, are explicitly resolved whilst
157 those smaller are modelled (Rodi et al. [41]). Hence, the governing equations
158 in LES are the spatially-filtered mass and momentum conservation Navier-
159 Stokes equations for incompressible viscous flow that read as:

$$\frac{\partial u_i}{\partial x_i} = 0 \tag{1}$$

$$\frac{\partial u_i}{\partial t} = -\frac{1}{\rho}\frac{\partial p}{\partial x_i} - \frac{\partial u_i u_j}{\partial x_i} + \nu \frac{\partial^2 u_i}{\partial x_j^2} - \frac{\partial \tau_{ij}}{\partial x_j} + \frac{1}{\rho}\frac{\partial p_0}{\partial x_i}\delta_{11} \tag{2}$$

160   Here u_i and x_i are the vectors of velocities and coordinates, p denotes
161 pressure, ν and ρ are the kinematic viscosity and density of the fluid respec-
162 tively, τ_{ij} represents the sub-grid scale stresses, and δ is the Kronecker delta.
163 Periodic streamwise flow condition (x_1) is adopted with a constant pressure
164 gradient p_0, which ensures uniform flow rate Q, applied only to the main
165 channel region, i.e. not applied to the lateral cavities region (Bomminayuni
166 and Stoesser [42]).
167   In Hydro3D, the computational domain is discretised as a rectangular
168 Cartesian mesh divided into smaller sub-domains which are inter-communicated
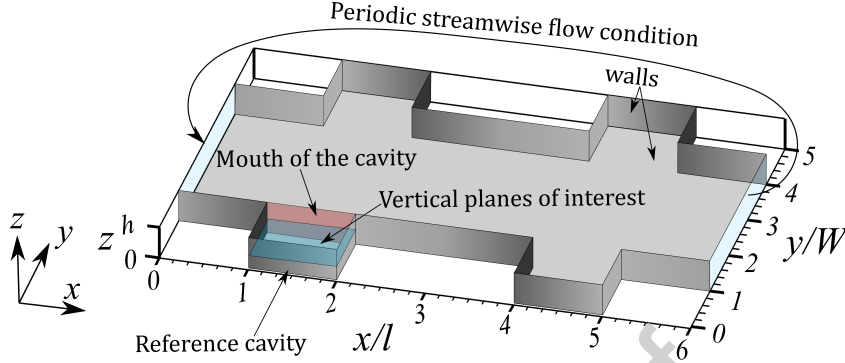
8

Figure 3: Geometric configuration of the computational domain which corresponds to configuration 2.1 in the laboratory work of Juez et al. [17]. Given the symmetrical and periodical characteristics of the physical system, two lateral embayments on each side were used when building the computational domain. A periodic streamwise flow condition is imposed in the main channel upstream and downstream ends.

via Message Passing Interface (MPI) to perform the simulation in parallel (Ouro et al. [34]). Staggered storage arrangement of velocities is adopted with fourth-order central differences to approximate velocity fluxes and the Poisson pressure equation is solved using a multi-grid technique (Cevheri et al. [43]). The simulation is advanced in time using a fractional-step method with a three-step Runge-Kutta method providing a second order accuracy in time. The Wall-Adapting Local-Eddy viscosity model from Nicoud and Ducros [44] is used to calculate the sub-grid scale stress tensor.

The computational domain spans 1.5 m long ($x/l = 6$) and comprises two cavities on each lateral boundary of the channel, as depicted in Figure 3. The simulations start with an initial uniform velocity field and run for several flow-throughs using inflow-outflow conditions to allow the flow to develop within the cavities and remove any transients in the main channel from the initial flow state. Thereafter, periodic streamwise conditions are applied, which represents a scenario of an infinite array of lateral cavities. At the bottom and lateral walls, a non-slip condition is imposed as the first computational grid cell is within the viscous sub-layer. The free-surface is treated as a shear-free rigid lid as the Froude numbers of the studied cases are below 0.5 (Constantinescu et al. [26], Koken and Constanstinescu [45]). Seiching across the channel was not observed during the experiments for the selected geometrical configuration herein chosen (Juez et al. [18]).

9

190 The resolution of the numerical grids is uniform across the whole domain
191 and details are provided in Table 2. For the two lowest discharges (Q1 and
192 Q2) the grid size is 1 mm, whilst for Q3 the same resolution is used in x-
193 and y-direction and that in the vertical increases to 0.5 mm, as the increase
194 in friction velocity due to higher flow discharge requires higher resolution to
195 have the first grid off the wall within the viscous sub-layer ($\Delta z^+ = \Delta z u_*/\nu <$
196 12, Rodi et al. [41]). The meshes comprise a total of 38.5, 55 and 154 million
197 elements for the different cases and the simulations run using between 100
198 and 300 CPUs on *Supercomputing Wales* facilities.

Case	Δx [m]	Δz [m]	Δz^+ [-]	u_* (LES) [m/s]	u_* (Exp) [m/s]	t_e [s]
Q1	0.0010	0.0010	6.91	0.014	0.018	2.53
Q2	0.0010	0.0010	8.73	0.017	0.021	2.86
Q3	0.0010	0.0005	5.06	0.020	0.024	3.46

Table 2: Details of the grid resolution in streamwise (Δx) and vertical (Δz) directions, vertical resolution in wall units (Δz^+), friction velocity (u_*) obtained from experiments and LES, and eddy turn-over time ($t_e = h/u_*$), for the flow configurations studied.

199 For the time integration in the LESs, variable time step is adopted with
200 constant Courant-Friedrichs-Lewy (CFL) value equal to 0.3 in order to guar-
201 antee numerical stability. As the bulk conditions of the three study cases are
202 different, the simulations run for an approximately equivalent physical time
203 of 190 eddy turn-over time, defined as $t_e = h/u_*$, representative of the time-
204 scale of the largest flow structures in the main channel. This criterion yields
205 to a total simulation times of 559 s, 620 s and 680 s in cases Q1, Q2 and Q3,
206 respectively. These time integration intervals are long enough to ensure con-
207 verged flow statistics. The LES-computed friction velocity presented in Table
208 2 is obtained from the time-averaged pressure gradient as $u_* = \sqrt{dp/dx R_h/\rho}$,
209 where R_h stands as the main-channel hydraulic radius and dp/dx is the time-
210 averaged pressure gradient imposed in the main channel to keep a constant
211 flow rate Q. LES consistently underpredicts the friction velocity by approxi-
212 mately 15% compared to the experimental value. This may be attributed to
213 the lack of modelling the concrete rough walls or representing an infinite ar-
214 ray of lateral embayments using periodic boundary conditions, which might
215 lead to slightly different flow conditions from those found in the experiments
216 at the measured location.
217 The analysis of the transport of momentum across the cavity opening is

10

²¹⁸ analysed using the LES results, evaluated with the contribution of each terms
²¹⁹ of the Reynolds-averaged momentum equation in y-direction, in which steady
²²⁰ conditions are assumed, i.e. $\partial V / \partial t = 0$. The adopted Reynolds-Averaged
²²¹ Navier-Stokes (RANS) equation in y-direction reads:

$$0 = \underbrace{-U\frac{\partial V}{\partial x}}_{\text{I}} \underbrace{-V\frac{\partial V}{\partial y}}_{\text{II}} \underbrace{-W\frac{\partial V}{\partial z}}_{\text{III}} \underbrace{-\frac{\partial u'v'}{\partial x}}_{\text{IV}} \underbrace{-\frac{\partial v'v'}{\partial y}}_{\text{V}} \underbrace{-\frac{\partial v'w'}{\partial z}}_{\text{VI}} \underbrace{-\frac{1}{\rho}\frac{\partial P}{\partial y}}_{\text{VII}} + \underbrace{\nu\left(\frac{\partial^2 U}{\partial x^2} + \frac{\partial^2 V}{\partial y^2} + \frac{\partial^2 W}{\partial z^2}\right)}_{\text{VIII}} \tag{3}$$

²²² Here the terms I, II and III represent the convective transport of y-axis
²²³ momentum, the momentum transport due to turbulent stresses correspond
²²⁴ to the terms IV to VI, term VII is the pressure gradient that drives the flow
²²⁵ into the cavity, and term VIII corresponds to the viscous stresses.

²²⁶ 3. Results

²²⁷ 3.1. Time-averaged flow

²²⁸ Time-averaged flow field developed in the reference cavity and in the
²²⁹ adjacent area of the main channel is presented in Figure 4 for the horizontal
²³⁰ plane at $z/h = 0.5$. Contours of mean streamwise (a) and transverse (b)
²³¹ velocities, streamwise (c) and transverse (d) turbulence intensities, Reynolds
²³² shear stress $u'v'$ (e) and turbulent kinetic energy (defined as $tke = u_i u_i / 2$)
²³³ (f), are shown for the flow conditions corresponding to case Q2. Results are
²³⁴ adimensionalised using the bulk velocity of the main channel, U_0, and shear
²³⁵ velocity, u_*.

²³⁶ Flow streamlines reveal that a single recirculating vortex (hereinafter de-
²³⁷ noted as Main Vortex (MV)) is formed within each cavity occupying most
²³⁸ of its volume governing the in-cavity flow, whilst secondary vortical struc-
²³⁹ tures of much smaller size are generated at the corners, forced by continuity
²⁴⁰ and the no-slip condition at the cavity walls. These can be deemed to have
²⁴¹ negligible influence on the hydrodynamics (Mignot et al. [15]). Maximum
²⁴² streamwise negative velocities are found near the wall opposite to the cavity
²⁴³ opening, reaching values up to $U \approx -0.25 U_0$. The in-cavity flow observed
²⁴⁴ corresponds to the skimming flow type due to its geometric aspect ratio near
²⁴⁵ the unity (Meile et al. [46]). In such flow type, the recirculating MV is
²⁴⁶ largely decoupled from the main stream flow and no interference between

11

²⁴⁷ cavities happens, which can be translated into reduced mass and momentum
²⁴⁸ exchange. Furthermore, typically if the aspect ratio is from 0.5 to 1.5, one
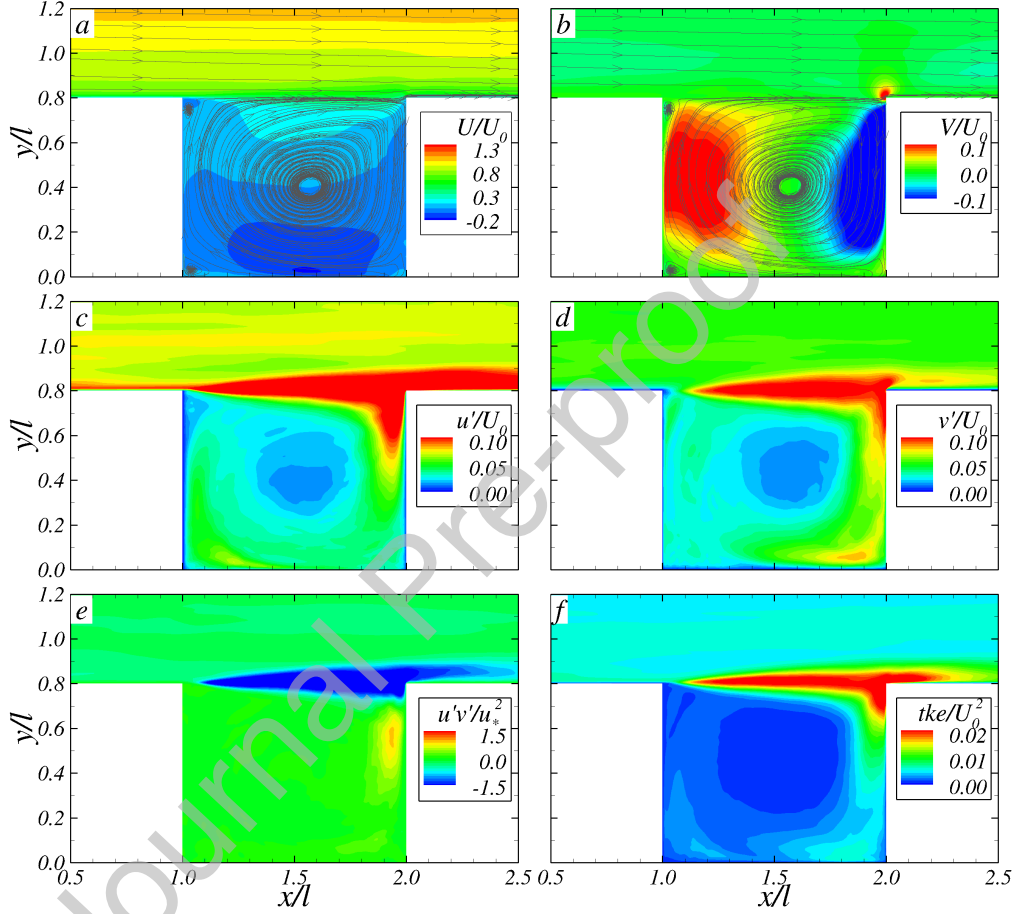²⁴⁹ single eddy is observed in the cavity.

Figure 4: Distribution of normalised time-averaged (a) streamwise (U/U_0) and (b) transverse velocities (V/U_0), (c) streamwise (u'/U_0) and (d) transverse (v'/U_0) turbulence intensities, (e) Reynolds shear stress ($u'v'/u_*^2$), and (f) turbulence kinetic energy (tke/U_0^2), for the case Q2 and for the horizontal plane at $z/h = 0.5$. Flow streamlines are only drawn in a and b for sake of simplicity.

²⁵⁰   Areas of large velocity fluctuations reveal high turbulence activity and
²⁵¹ second-order statistics are observed to be maximum across the shear layer
²⁵² generated between the cavities and the main channel, i.e. $y/l = 0.8$, with
²⁵³ nevertheless some degree of penetration into the cavity near the downstream

12

254 inner wall. In the contribution to turbulent kinetic energy, u' values are
255 found larger than v' across the mouth of the cavity even though momentum
256 exchange between main stream and cavities seems to be predominantly in
257 the transverse direction. Regions of large u' are also observed across the
258 main channel lateral wall at downstream of the cavities. These fluctuation
259 of streamwise velocities are due to the coherent structures recurrently shed
260 in the shear-layer as depicted in Figure 1 and presented later in Section
261 3.2. Inside the cavity, minima of velocity fluctuations are attained close to
262 the core of the recirculating MV suggesting that this is mostly stationary in
263 time without major spatial oscillations across the cavity region, as commonly
264 found in skimming flows (Weitbrecht et al. [11]). Contours of Reynolds shear
265 stress reveal the shear layer grows in size since the upstream outer corner and
266 reaches its widest distribution close to the downstream cavity corner (Mignot
267 et al. [15]).

268 A key aspect in the simulation of embayment flows is the prediction of
269 the position of the core of the recirculating main vortex, MV, since this is
270 somewhat related to the sedimentation patterns which are observed in the
271 cavity bottom. Figure 5 presents the relative coordinates $(x/l, y/W)$ of the
272 recirculating vortex core for two extreme positions in the water column, i.e.
273 water surface $(z = h)$ and cavity bottom $(z = 0)$. These positions were
274 determined based on the streamlines of mean flow from LES (e.g. Figure
275 4a). In the same figure, the position of the MV core for the surface observa-
276 tions made in the experimental work with surface PIV (Juez et al. [17]) are
277 represented as well.

278 The 3D nature of this vortical structure is obvious confirming the results
279 by Tuna et al. [47]: the superficial position of the main vortex does not match
280 the position of the core of the vortex close to the bottom. Taking into account
281 the vertical variation, for case Q1, the shift in the core position is small. On
282 the contrary, for the two higher discharges and water depths (Q2 and Q3),
283 the vortex centre moves towards the mouth of the cavity with increasing
284 submergence. The largest change in the core position is observed for the
285 highest Reynolds number case, i.e. Q3. A trend with the flow is observed
286 for both the numerical and laboratory results: when becoming shallower, the
287 core of the vortical structure approaches the cavity entrance. Overall, a good
288 agreement is found between computational and experimental data, with the
289 LES predicting the x-locations within a 4% error margin and within a 10%
290 accuracy for $y-$coordinates.

291 The distribution of the mean flow across the transition plane between the
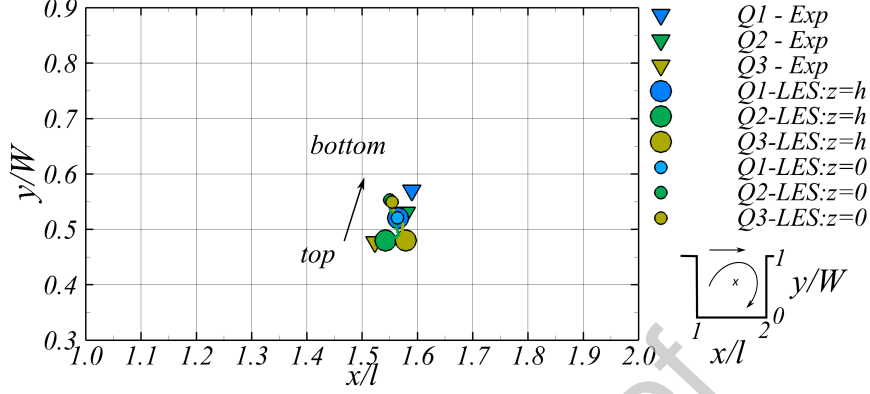
Figure 5: Zoom-in of the location of the recirculating main vortex core position obtained from time-averaged velocities computed with LES and experimental measurements from Juez et al. [17].

main stream and the lateral cavity is presented in Figure 6 for the three cases withh contours of streamwise and transverse velocities. A similar pattern of U/U_0 is developed in cases Q2 and Q3, in which the largest velocities are found in the downstream half with maximum values attained near the bottom and at the free-surface. In case Q1 there seems to exist a more uniform distribution of the maximum velocity through the channel-cavity transitions section, which is a consequence of shallowness.

The spacial region of maximum negative cross-flow velocities V/U_0 appears to be similar among cases, specifically at $1.2 < x/l < 1.9$, at $z/h \approx 0.3$ for Q2 and Q3, whilst for Q1 a slightly higher position is found of $z/h \approx 0.4$. The cross-flow mean velocity V here measured is the main responsible for exchange of mass and momentum between the cavities and the main channel by the mean flow. The negative V-velocity areas identify where mass entrains into the cavity (Sanjou and Nezu [48]). Conversely, mass flush out mainly occurs at two locations, across the entire water depth near the downstream cavity wall at $x/l > 1.9$ and, with lower velocity values, between $0.2 < z/h < 0.9$ in the upstream half of the cavity mouth section. Note that for cases Q2 and Q3, in the region of $1.8 < x/l < 1.9$, entraining flow is found across the water column while this is not observed in the case with the lowest discharge.

Figure 7 shows second-order flow statistics, only for case Q2 for the sake of brevity. The mostly 2D distribution of the three components of turbulence intensity and the turbulent kinetic energy reveal that the flow near
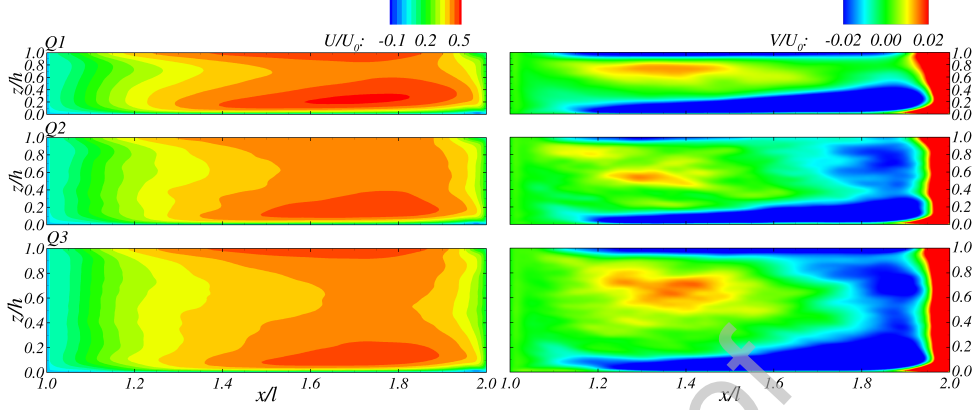
14

Figure 6: Distribution at a plane through the mouth of the cavity at $y/W = 1.0$ (cf. Figure 3) of the normalised time-averaged streamwise (U/U_0) and transverse (V/U_0) velocities for the three cases.

the upstream corner of the cavity is less turbulent while, after a distance of $x/l = 1.2$, the turbulence activity in this pane grows. Lower levels of turbulence are observed near the channel bed and free-surfaces. Contours of Reynolds shear stresses $u'v'$ along the mouth of the cavity feature negative values with an almost uniform distribution in the vertical direction. The growing turbulence activity from the upstream towards the downstream cavity wall is in agreement with the development of the shear layer sketched in Figure 1 and visible in Figure 4, which is the expected main region of turbulence production in this flow.

Qualitative comparison of velocities at the free-surface layer between LES and experiments is presented in Figure 8, with profiles of U/U_0 and V/U_0 along transverse locations $x/l = 1.25$ and 1.50 for the three cases. Distribution of U shows that negative velocities are found for $y/W < 0.5$ for most cases, as expected from the contours of U in Figure 4a. While in the mid region of the cavity LES agrees well with the PIV data, discrepancies are observed near the wall opposite to the mouth of the cavity, i.e. $y/W = 0.0$. This is attributed to the known difficulty for the 2D-PIV to provide accurate velocity estimates near the walls, due to the decreasing concentration of tracer particles and the strong flow gradients near the walls, these velocity measurements are usually biased (Kähler et al. [49]). Profiles of transverse velocity show nevertheless a good match between computational and experimental data at both locations for all the studied cases.
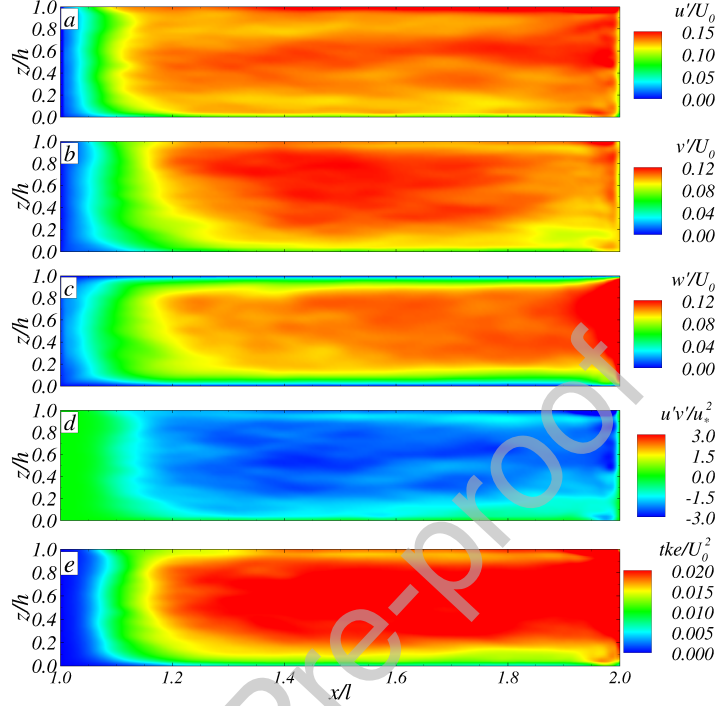
15

Figure 7: Distribution at a plane through the mouth of the cavity at $y/W = 1.0$ (cf. Figure 3) of the (a) streamwise (u'/U_0), (b) transverse (v'/U_0) and (c) vertical (w'/U_0) turbulence intensities, (d) Reynolds shear stress ($u'v'/u_*^2$) and (e) tke/U_0^2, for the case Q2.

3.2. Instantaneous turbulent flow structures

The turbulent mechanisms of mass and momentum exchange between the main channel and the lateral cavities are conditioned by the coherent structures which form in the shear layer and penetrate inside the cavities.

Figure 9 presents the turbulent structures deduced with iso-surfaces of instantaneous pressure fluctuation, $p' = p - P$, and coloured with streamwise velocity for half of the channel width for the case Q2. A broad spectrum of flow structures travelling through the main channel is observed with the largest ones advected along the middle of the main channel cross-section. Closer to the side walls the size of the turbulent structures reduces notably. Of great interest are the Kelvin-Helmholtz (KH) vortices developed in the shear layer at the mouth of the cavities as a consequence of the velocity difference between the low-velocity cavity flow and higher-velocities in the main stream. In their inherent 3D shape, KH vortices appear to keep a fairly co-
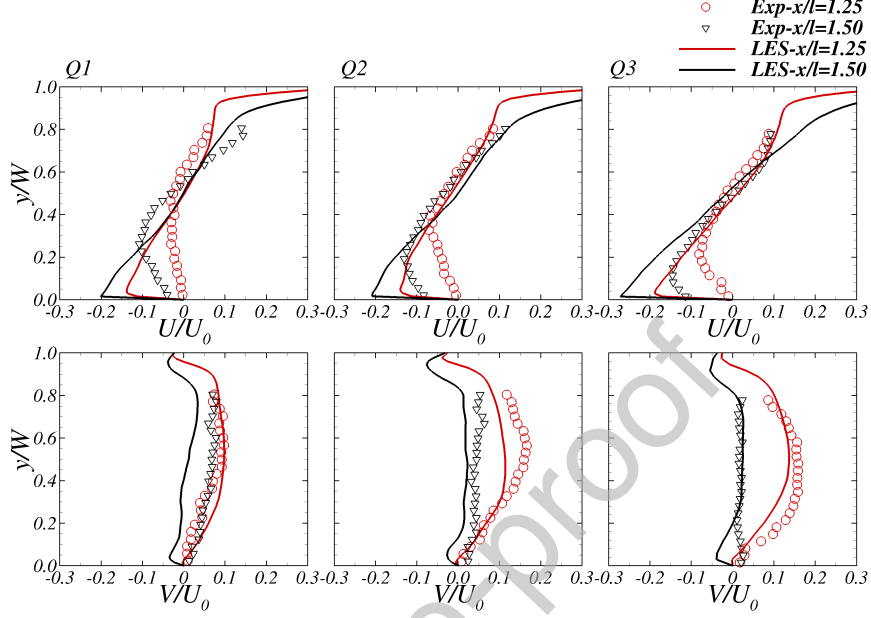
16

Figure 8: Transverse profiles of streamwise (U/U_0) and transversal (V/U_0) velocities at $x/l = 1.25$ and 1.50. Comparison between experiments (Juez et al. [17]) and present LES results.

herent vertical structure across the water depth while convected downstream, as no large velocity gradients in the vertical direction are observed (Mignot et al. [50]). Such coherent shape is more consistent for case Q1 as the flow is shallower. Furthermore, the large-scale MVs occupy the entire embayments volume with vertically-evolving loci at relatively similar position over the cavity cross-section, as depicted in time-averaged streamlines in Figure 4.

At the internal cavity corners secondary recirculating vortices are observed, which, as previously mentioned, are forced by continuity and by the shear between the MVs and sidewalls. Note that their size is considerably smaller than the MVs and, consequently, their influence in the hydrodynamics of the in-cavity flow, and the processes of exchange of mass and momentum between the cavity and the mains channel which are here under analysis, can be deemed negligible (Weitbrecht et al. [11]).

Figure 10 displays contours of instantaneous pressure, p, with vectors of 2D velocities with magnitudes ($0.2 \cdot u,v,0$) at a plane located at $z/h = 0.5$ for the flow conditions corresponding to the highest discharge, Q3, with a
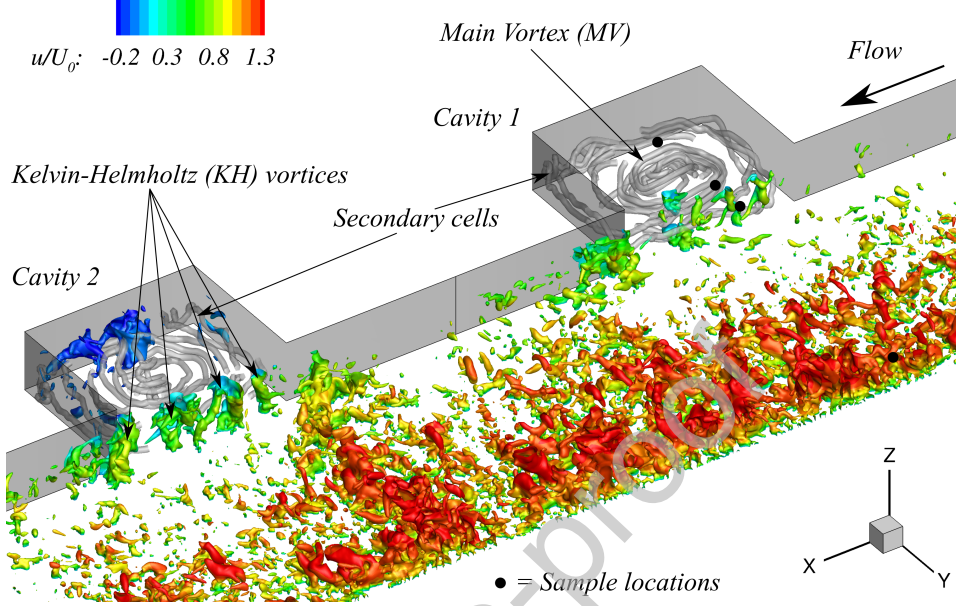
17

Figure 9: Instantaneous flow structures represented with iso-surfaces of pressure fluctuation p' coloured with normalised streamwise velocity for the case Q2. Only half of the channel width is displayed.

time lapse of 0.40 s between each consecutive snapshots. Here the two points located at $x/l = 1.5$ at $y/W = 0.875$ and 1.125 are included as they are used to collect pressure signal time series for the shear layer instability analysis in the spectral domain. At the upstream corner at $t = t_0$, the onset of the shear layer instabilities occurs as a result of the velocity gradients between regions (Mignot et al. [50]). In their early formation stages, the Kelvin-Helmholtz (KH) structures are relatively small but, as they are convected downstream, grow in size due to the interaction with the ambient flow and travel with an almost parallel direction to the cavity mouth transverse plane. For this reference cavity on the right-hand side of the main channel, KH vortices feature a clockwise rotation as a consequence of them being fed at their front edge by transversal velocities from the main channel moving into the cavity and at their trailing edge by those velocities being flushed out from the cavity. During the last stages of their downstream advection, KH vortices progressively loss coherence until impinging the downstream cavity corner, when they partially entrain into the cavity or continues with the main stream (Rockwell and Knisely [51]). This is the main process of turbulent transport

18

383 scalars between cavities and the main channel, as previously reported in
384 Mignot et al. [15] for square-like single cavity flows and Constantinescu et al.
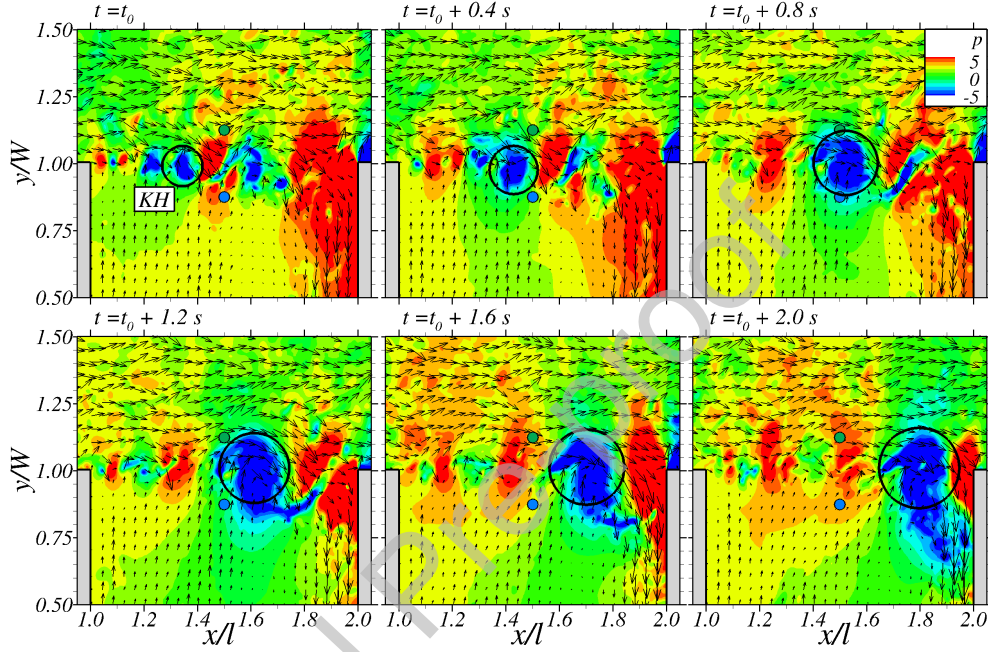385 [26] for scalar mixing in a series of groynes.

Figure 10: Contours of instantaneous pressure, p, with velocity vectors of components $(0.2 \cdot u, v, 0)$ at a plane located at $z/h = 0.5$ for the flow conditions corresponding to the highest discharge, case Q3. The snapshots have a time lapse of 0.40 s among them.

386 3.3. Spectral analysis of the variations in the pressure field

387 The results on the pressure field measured within the flow can reveal
388 whether standing wave (SW) phenomena occur and whether there is a co-
389 herent pattern in the temporal generation of KH vortices travelling across
390 the shear layer. As found in Wölfinger et al. [52], when the frequency of the
391 standing wave, f_{SW} and that of the shear-layer vortex shedding f_{SL} coincide,
392 a lock-on phenomenon is experienced. Under these resonance conditions, the
393 hydrodynamics of the in-cavity flow can dramatically change, modifying the
394 mass and momentum exchanges between the main channel-cavities. Juez
395 et al. [17] showed that under such conditions the in-cavity sedimentation
396 processes can be also completely altered. The standing waves that appear

19

₃₉₇ in enclosed water domains are called seiches. Whilst f_{SL} depends on the ge-
₃₉₈ ometry of the cavity and flow conditions (Wölfinger et al. [52]), f_{SW} can be
₃₉₉ approximated to be the eigenfrequency of the first eigenmode of the standing
₄₀₀ wave, f_1, determined as:

$$f_1 = \frac{\sqrt{gh}}{2B} \tag{4}$$

₄₀₁ To quantify the differences in the variation of the pressure field at different
₄₀₂ locations in the transversal direction (y-direction), spectra of the pressure
₄₀₃ time-series, at the four sample locations located at $y/W = 0.125$, 0.875,
₄₀₄ 1.125 and 2.500 at mid water depth and depicted in Figure 9, are computed
₄₀₅ and presented in Figure 11. These locations are aligned with the cavity
₄₀₆ centre ($x/l = 1.5$) transverse to the main flow direction, as depicted in Fig.
₄₀₇ 10, allowing to determine the relevant oscillating phenomena conditioning in
₄₀₈ flow field.

₄₀₉ At frequencies in inertial region and above, all the spectra feature two
₄₁₀ outstanding regions of slopes -5/3 and -3. These results suggest the existence
₄₁₁ of quasi-2D vortical structures that follow an inverse turbulent energy cascade
₄₁₂ (Nikora et al. [53], Sommeria [54]): energy transfer from the small eddies
₄₁₃ towards the large vortical structures is verified. Such turbulent dynamics
₄₁₄ corresponds to those observed in Figure 10 in the shear layer region where
₄₁₅ small eddies are formed, advected downstream, and coalesce to form larger
₄₁₆ turbulent structures.

₄₁₇ For high frequencies, in the region of the inverse cascade (with -3 slope)
₄₁₈ and regardless the flow conditions, the spectra at the four different transverse
₄₁₉ locations collapse with the same level of energy. However, for lower frequen-
₄₂₀ cies, the energy decay observed for the case Q1 is quite different between the
₄₂₁ points inside of the cavity, i.e. $y/W < 1.0$, and those outside. These obser-
₄₂₂ vations for Q1, when compared with the cases Q2 and Q3, suggest that there
₄₂₃ is a separation between the turbulent dynamics between the inner and outer
₄₂₄ regions of the cavity for shallower flows. At the dissipative scales, when the
₄₂₅ flow tends to isotropy, this difference is not seen anymore due to a similar
₄₂₆ spectral energy decay found in all cases.

₄₂₇ Two notable peaks are always observed in the production range of the
₄₂₈ spectra presented. One corresponds to shedding frequency of the KH vortices
₄₂₉ produced in the shear layer region while a second energy peak corresponds
₄₃₀ to the standing wave. For the case Q1, one of the peaks is common to the

431 three positions inside and the verge of the cavity: $y/W = 0.125$, 0.857 and
432 1.125. A second energy peak at higher frequency is observed for all the four
433 positions, including $y/W = 2.500$, at the centre of the main channel. At the
434 latter location, a signature from the KH vortices in the pressure signal is
435 not expected according to the pressure field observed in Fig. 10. Hence, the
436 first peak at lower frequency (f_{SL}) is attribute to the shear layer KH vortices
437 shedding and the second peak at higher frequency (f_{SW}) to the standing
438 wave which should be felt in the pressure field across the channel: $f_{SL} =$
439 0.72 Hz and $f_{SW} = 1.17$ Hz respectively, for case Q1. For the cases Q2 and
440 Q3, values of frequencies f_{SL} and f_{SW} increase with increasing flow rate and
441 decreasing shallowness.

442 Frequencies f_{SL} and f_{SW} computed for the different cases are summarised
443 in Table 3 together with values of f_1 (Eq. 4). The ratio between f_{SL}/f_{SW} are
444 lower than the unity, although approaching this value with increasing flow
445 rate, which suggests that both unsteady phenomena are not coupled, similar
446 to the *pre lock-on* case in Wölfinger et al. [52]. For discharges higher than
447 the ones tested, an interaction between the standing wave and shear-layer
448 shedding is expected.

449 The ratio between the standing wave frequency from the numerical simu-
450 lations (f_{SW})with the theoretical standing-wave value (f_1) are close or above
451 four, indicating that for all the studied cases no amplification of the effect
452 of the standing wave due to resonance is expected, i.e. when $f_{SW} \approx f_1$.
453 These results are confirmed with the lack of seiching observed during the
454 experiments reported in Juez et al. [18].

455 Finally, in Table 3 values of the reduced velocity, defined with the bulk
456 velocity and main channel width as $U_r = U_0/(f_1 B)$, for the three cases
457 Q1, Q2 and Q3 are presented. As U_r is lower than the unity which again
458 indicates that non-resonance conditions are expected. In the experimental
459 work by Wölfinger et al. [52], for a single lateral cavity with similar Reynolds,
460 Froude numbers and reduced frequency, analogous *pre lock-on* transient flow
461 behaviour was found.

462 Four ranges can be identified in the spectral distribution of the pressure
463 signal, as depicted in Figure 12 for Q2 at two sample locations, one inside the
464 cavity and another in the main channel centreline. At the lowest frequencies,
465 typically larger than the shear-layer shedding frequency, the energy produc-
466 tion range "I" is found. The range "II" is characterised by an energy decay
467 that follows a -1 slope, which was not drawn in Figure 11 for clarity purposes.
468 Nikora [55] linked the -1 slope to the superposition of vortical structures in
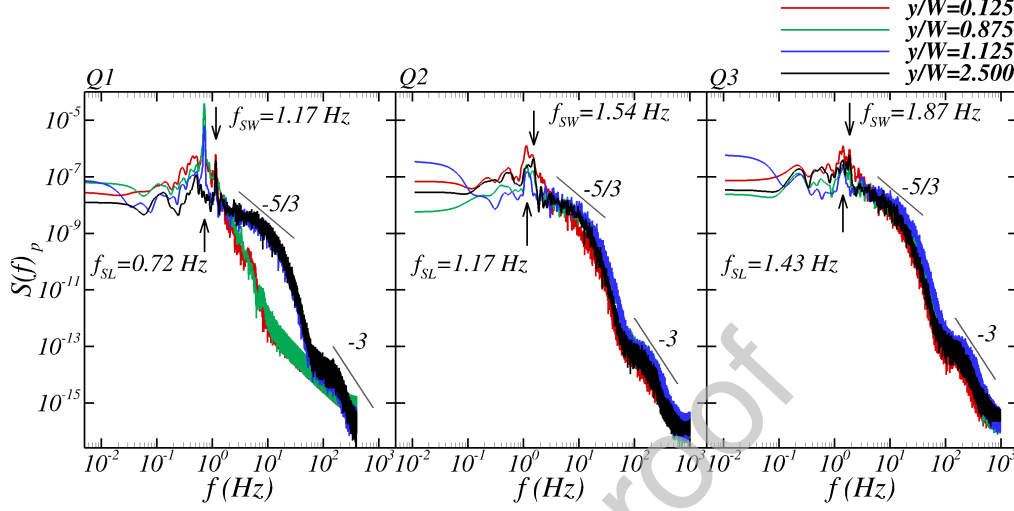
21

Figure 11: Power spectral density computed from pressure time-series at four spatial samples located at different transverse locations and depicted in Figure 9, for $x/l = 1.5$ and $z/h = 0.5$ (see Figure 9) and for all the studied cases Q1, Q2 and Q3.

Case	h [m]	f_{SW} [Hz]	f_{SL} [Hz]	f_1 [Hz]	f_{SL}/f_{SW} [-]	f_{SW}/f_1 [-]	U_r [m/s]
Q1	0.035	1.17	0.72	0.29	0.61	3.99	0.76
Q2	0.050	1.54	1.17	0.35	0.76	4.40	0.84
Q3	0.070	1.87	1.43	0.41	0.77	4.51	0.86

Table 3: Values of water depth, frequencies of shear layer vortex shedding (f_{SL}), standing wave (f_{SW}), approximated standing wave (f_1) and their ratio and reduced velocity (U_r) for the three cases. Values of the frequency of the shear layer (f_{SL}) and standing wave (f_{SW}) were obtained through the signal analysis displayed in Figure 11. The value of the approximated standing wave (f_1) was computed by means of Eq. 4.

⁴⁶⁹ the energy cascade process. It is in this spectrum interval in which energy
⁴⁷⁰ peaks at f_{SL} and f_{SW} are found. In the inertial sub-range "III", the energy
⁴⁷¹ decay follows the -5/3 slope as previously shown in Figure 11. At frequencies
⁴⁷² in the order of 10^2 Hz the dissipation range "IV" takes place, which features a
⁴⁷³ -3 slope owed to the inverse cascade process commonly found in shallow flows.
⁴⁷⁴ Kraichnan [56] justified that both -5/3 and -3 slopes can be simultaneously
⁴⁷⁵ present in the energy spectrum of two-dimensional flows, being the former
⁴⁷⁶ a consequence of the largest flow scales transferring kinetic energy from low
⁴⁷⁷ to high frequencies, whilst the latter is due to the small scales feeding the
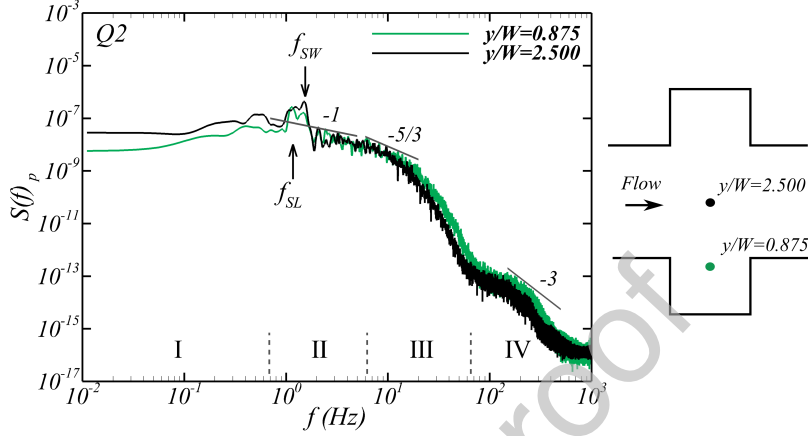
22

478 larger ones.

Figure 12: Identification of the main ranges and slopes found in power spectral density computed from pressure time-series. Samples are located inside ($y/W = 0.875$) and outside ($y/W = 2.5$) of the cavity at $x/l = 1.5$ and $z/h = 0.5$, for the case Q2.

479 The intrinsic high-resolution of the simulations is evidenced thanks to
480 the full palette of frequencies resolved. It is noteworthy that the present
481 LES capture remarkably well the presence of the standing wave effect in the
482 pressure field, despite adopting a rigid-lid approximation without explicitly
483 resolving the free-surface motion. The sub-grid scale (sgs) model, responsible
484 for taking into account the flow scales lower than the grid resolution, does
485 not introduce any additional dissipation until frequencies in the order of 10^3
486 Hz. This small interplay of the sgs model is also quantified with the ratio of
487 the sgs to kinematic viscosity, which attains values lower than the unity in
488 most of the computational domain.

489 *3.4. Momentum transfer between main channel and lateral cavities*

490 Governing processes in the momentum transfer between the main channel
491 and lateral cavities are analysed looking at the components of the Reynolds
492 Averaged Navier-Stokes (RANS) momentum equation in the spanwise direc-
493 tion (y-RANS), defined in Eq. 3. The embayments under analysis have a high
494 aspect ratio, which means that the flow is expected to be of the skimming
495 type as described in Meile et al. [46]. The aspect ratio corresponds to the
496 case of the so-called "closed" cavity in Meile et al. [46]. Under this scenario,

23

the entrainment of main-channel streamwise momentum is limited, in oppo-
sition to what occurs in lower-aspect ratio geometries, i.e. with relatively
larger cavity opening length.

The scale over which the terms in y-RANS equation are time-averaged is
sufficiently large to ensure statistically convergence of second-order moments.
This means that the instantaneous flow structures developed in the shear
layer, said to be responsible for mass and momentum exchange (Weitbrecht
et al. [11], Constantinescu et al. [26]), are accounted within the turbulent
stresses of the flow. Cross-sectional mean values of the y-RANS equation
are integrated over the mouth of the cavity plane are shown in Figure 13 for
the three cases normalised by l/U_0^2. Positive values indicate flushing out of
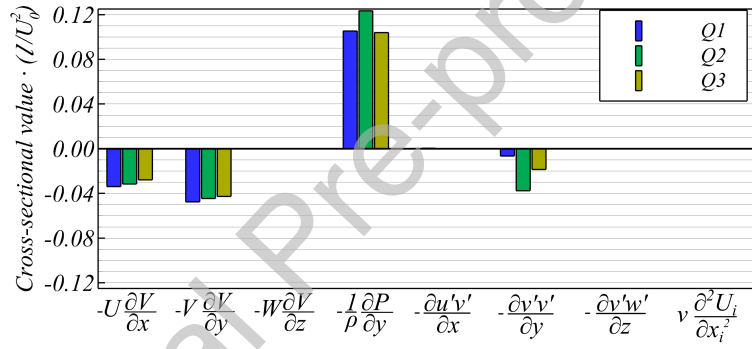momentum whilst negative denote its entrainment into the cavity.

Figure 13: Components of the terms of the y-RANS equation, spatially averaged over the
mouth of the cavity plane, for the three cases Q1, Q2 and Q3.

The results show that the pressure gradient is the only term responsible
for driving the momentum out the cavity into the main channel. On the
other hand, terms involved in the entrainment of momentum from the main
channel to the cavity are mainly the convection terms $U\partial V/\partial x$ and $V\partial V/\partial y$
and, to a lesser extent, the $v'v'$ Reynolds stress. The gradient of the tur-
bulent momentum flux $u'v'$ has a negligible contribution to the transverse
momentum exchange so does the viscous terms, as expected due to the high
Reynolds number of the flow.

There is a similar pattern in the y-RANS results integrated over the
mouth of the cavity for the three flow conditions. However, in the case Q2,
there is a larger contribution from the pressure gradient counterbalanced
by an additional larger gradient of turbulent flux $v'v'$, being the convection

24

521 terms of the mean flow field very similar to those in Q1 and Q3. These
522 results imply that the momentum exchange mechanisms vary depending on
523 the flow conditions for the same cavity configuration. This agrees with the
524 results on the sediment trapping efficiency obtained in the experimental work
525 by Juez et al. [17]. In their case, for the present high-aspect ratio geometry,
526 the maximum efficiency was attained for Q2 and close values were obtained
527 for Q1 and Q3, indicating a clear relation between momentum and sediment
528 exchanges between the main channel and the cavities.

529 The distribution of the four main terms from the y-RANS equation across
530 the mouth of the cavity is presented in Figure 14 for the case Q2. It is
531 observed that the convective term $U\partial V/\partial x$ aids to momentum entrainment
532 (negative values) in the 20% downstream part of the cavity whilst positive
533 values are mostly found between $1.5 < x/l < 1.8$. The term $V\partial V/\partial y$ features
534 only two region of large positive values, namely near the channel bottom and
535 free-surface, indicating the regions where momentum is transported from the
536 cavity to the main channel.

537 Near the downstream wall, the convective terms corresponding to the
538 mean flow have large negative values contribute all in the same direction
539 of transverse momentum entrainment. The turbulent stress term, together
540 with the convective ones, contribute to the net transport of spanwise mo-
541 mentum from the main channel into the cavity, and this is well-observed in
542 its distribution over the mouth of the cavity which exhibits mostly negative
543 values.

544 Finally, the pressure gradient contours in Figure 14 show its positive
545 contribution counterbalancing the turbulent term in the region $1.1 < x/l <$
546 1.5, and between $1.85 < x/l < 2.0$ the convective terms.

547 *3.5. Mass exchange*

548 Exchange of mass processes between the high-momentum main channel
549 and lateral embayments vary depending on the geometric characteristics of
550 the cavity. The present cavities feature an aspect ratio W/l equal to 0.8
551 (i.e. skimming flow type) implying there is no entrainment of the main
552 channel flow into the cavity. The exchange velocity E across the channel-
553 cavity interface is defined as the cross-sectional average value of the absolute
554 transverse velocity, and the exchange coefficient k relates the former exchange
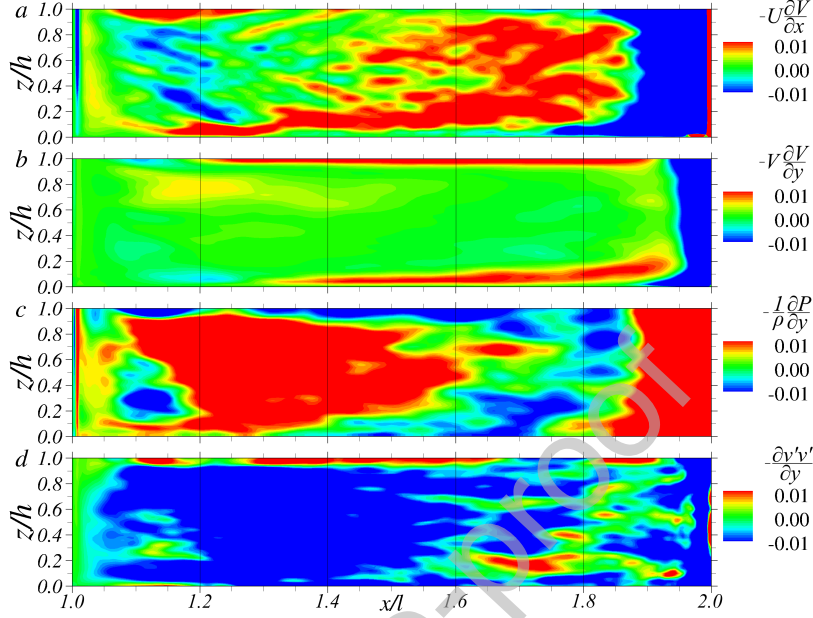555 velocity with the bulk velocity, which read as:

Figure 14: Distribution along the cavity mouth of the main y-RANS equation components for the Q2 case.

$$E = \frac{1}{Wl} \int_0^l \int_0^W |V| dz dx \tag{5}$$

$$k = \frac{E}{2U_0} \tag{6}$$

Table 4 presents the exchange coefficient values, k, obtained in the experiments of Juez et al. [18], those computed from the LES integrated across the mouth of the cavity at $y/W = 1.0$ (see Fig 6), and also those obtained from LES using the values of $|V|$ at the domain top lid. The latter values are calculated similarly to the experimental entrainment coefficients which were obtained by using PIV measurements at the water surface. The experimental and numerical entrainment coefficients differ notably, and only the k values at LES-top display values with the same order of magnitude as the ones displayed in the laboratory. Disparity in the results of k between experiments and numerical predictions have previously been reported in Constantinescu et al. [26] in which k was estimated from contaminant decay. Furthermore, k

26

567 values obtained with PIV decrease when the flow discharge increases (from
568 Q1 to Q3). This agrees with Mignot et al. [15] but not with the results
569 reported in Weitbrecht et al. [11]. However, in Weitbrecht et al. [11] seich-
570 ing was not observed. Regarding the magnitude of the values, k (PIV) and
571 k (LES-top) display similar values to those obtained in Weitbrecht et al.
572 [11], Mignot et al. [15].

Case	k (PIV)	k (LES)	k (LES-top)
Q1	0.043	0.0081	0.0145
Q2	0.029	0.0090	0.0140
Q3	0.015	0.0084	0.0147

Table 4: Values of the dimensionless exchange coefficient obtained during the experiments of Juez et al. [18] using PIV, and computed with LES using velocities across the cavity-opening plane and those at the free-surface.

573 Despite the shallow nature of the flow, the turbulent structures that de-
574 veloped in the shear layer display 3D turbulent characteristics. Figure 9
575 presents the turbulent structures plotted with iso-surfaces of pressure fluctu-
576 ation. The turbulent structures in the vicinity of the shear layer are mainly
577 contained within the main channel. The observed 3D turbulent structures
578 behave as a vertical barrier avoiding the in-cavity development of the shear
579 layer (McCoy et al. [25]). This is an important observation, since the mass
580 exchange of fine sediments, pollutants or nutrients between the main chan-
581 nel and the cavities is thus notably limited/governed by the production of
582 turbulence in this region of the channel.
583 During the experimental campaign carried out in Juez et al. [17] plane
584 view photos of the in-cavity sedimentation patterns were taken at the end of
585 the experiment. These photos were treated to extract the surface occupied
586 by the sediments. Figure 15 presents iso-surfaces of time-averaged vertical
587 velocities $W/U_0 = \pm 0.1$, contours of turbulent kinetic energy (tke) at $z/h =$
588 0.01, and the areas corresponding to where the sediments settled at the end
589 of the experiments. Sediment deposition areas mostly coincide with those
590 lacking large vertical velocities implying that near-bed vertical velocities are
591 responsible for keeping them in suspension. Negative iso-surfaces of W are
592 found close to the lateral walls whilst positive values are mainly in the inner
593 recirculation area. Additionally, deposition areas also seem to correlate with
594 those where turbulent kinetic energy values are also small. These results
595 indicate that sediment particles are able to settle when vertical velocities
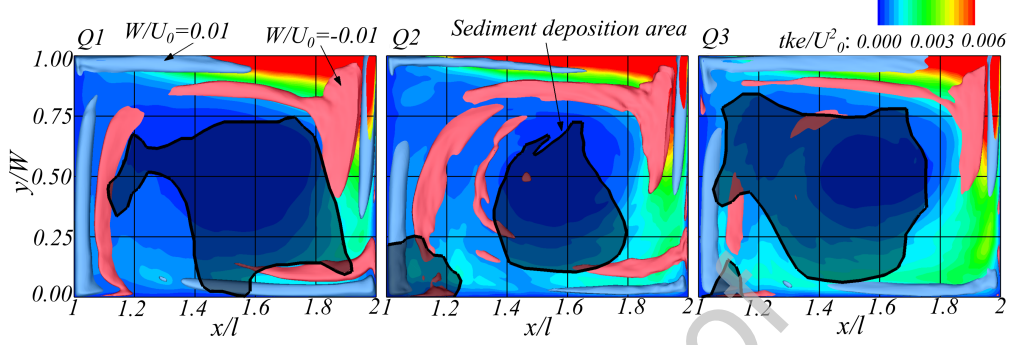
27

596 and turbulence are very low.

Figure 15: Comparison of the sediment deposition regions (shaded areas) obtained during the experimental campaign (Juez et al. [17]) with the computed flow field near the bottom bed of the cavity. Contours of turbulent kinetic energy are at $z/h = 0.01$ and iso-surfaces of vertical velocities show values $W/U_0 = \pm 0.1$. Note that only velocity iso-surfaces at $z = 7$ mm and below are shown.

4. Main Findings

598   The current research adopted high-resolution LES to identify and quantify
599 the major role played by the vortical structures characteristic of in-cavity
600 flows, specifically: vertically-oriented vortical elements generated in the shear
601 layer; a main recirculating in-cavity vortex; and small-scale in-cavity vortices.
602 Results of the hydrodynamics revealed that the flow within the cavities are
603 reasonably shallow with their flow dynamics largely dominated by a large-
604 scale structure, named as Main Vortex (MV), which extends over most of
605 this confined region. The appearance of a single MV is due to the relatively
606 squared shape of the cavities, resembling to a skimming flow type in which the
607 entrainment of momentum from the main stream into the macro-roughness
608 elements is reduced. While this energetic flow structure is expected to feature
609 a quasi-2D shape owed to the shallow flow conditions, the vertical position
610 of its core is proven to vary with depth, especially for the deeper case. It is
611 closer to the opening of the cavities near the bottom, whilst moving towards
612 to the opposite wall at the free-surface.

613   The velocity differences in the transition between the high-momentum
614 main channel and low-velocity cavities leads to the formation of shear layers,
615 in which a train of coherent vortices develops due to Kelvin-Helmholtz (KH)

28

instability. In spite of the shallow nature of the flow, these structures feature
a 3D nature occupying the whole water column (see Figure 9). These KH
vortices are smaller than the MV and travel over the mouth of the cavity
plane affecting both the in-cavity flow and the adjacent main channel region.
During their convection, they increase in size while remaining coherent until
impinging the downstream cavity wall (Figures 9 and 10). A fairly uniform
distribution of the Reynolds stresses over the whole water depth and across
the channel-cavity transition is also observed due to this coherence. At the
last stage, when impinging the downstream corner of the cavity, the KH
vortices breakdown, partially entraining into the cavity or going away with
the main stream.

As a result of this activity and dominance of the KH vortices, the mass
exchange between the main stream and in-cavity flow is limited and, con-
sequently, the dimensionless exchange coefficients computed with LES are
lower than the ones obtained with the surface PIV (see Table 4). LES re-
sults show the largest transverse velocities across the mouth of the cavity are
found in mainly two pockets extending across most of the streamwise length
of the embayment but confined at vertical locations near the free-surface and
bottom bed (Figure 6). Such velocity distribution highlights that the mass
exchange between the main channel and cavities is largely heterogeneous.
Hence, it is therefore inaccurate to assume that the flow patterns observed
at the water surface can precisely determine the mass exchange between the
main flow and lateral embayments.

LES captures recurrent temporal oscillations in the pressure fluctuations
across the entire channel, despite a shear-free rigid-lid condition is imposed at
the free-surface. At several sample locations distributed across the channel
width, a peak in the spectral energy distribution of the pressure signal is
observed at frequencies close to those of the theoretical standing wave. In
addition, spectra inside of the cavity revealed that shear-layer phenomena
affect the dynamics of the in-cavity flow and adjacent region of the main
channel, which was observed in the pathway of KH vortices during their
advection (Figure 10). The spectral analysis also reveals that the energy of
the quasi-2D MV is fed by the smaller scale structures from the shear layer,
observed in the -3 slope of the spectra in the dissipation range. Conversely,
the energy decay of the largest flow structures follows a -1 slope until the
inertial sub-range is reached.

The momentum transfer between the main channel and cavities is anal-
ysed with the Reynolds Averaged momentum equation in the cross-flow direc-

29

tion. The integration of each of the involved terms across the main channel-cavity transition plane reveals a large impact of the pressure gradient in the transverse momentum exchange. This appears to be the sole responsible for the momentum flush-out from the cavities to the main stream, mostly counterbalanced by the convective terms with a reduced contribution of the Reynolds normal stresses. Such key role of the pressure field in the momentum balance together with the fact that the shedding frequency of shear-layer KH vortices is nearly coupled with the standing-wave frequency, can be linked to the relevance of the seiche phenomenon in the sediment transport.

The turbulent flow characteristics computed inside the cavities served as a proxy to determine the sediment exchange reported in the laboratory experiments in Juez et al. [17]. The LES-predicted patterns of iso-surfaces of vertical velocities are linked to pathways of sediment movement: the sediment deposition areas are bounded by regions in which vertical velocities are lower than 1% the bulk velocity and levels of turbulent kinetic energy are very low. These findings reflect that the ease of the sediments to deposit within the cavity relies on the secondary flow distribution and its unsteadiness.

A key finding from this study is that low-frequency transverse pressure changes arises as an essential factor in the sediment transport in river bank lateral cavity flows. This variable is normally absent in experimental tests with PIV or ADV and normally omitted in the analysis. Such importance becomes crucial to understand why sediment transport dynamics change when seiching is present [47]. This, combined with the coupling of the standing wave and shear-layer KH vortices shedding that can further amplify the pressure field oscillations, determine when a given lateral embayment geometry performs best to trap sediments from the main channel, as previously observed in experimental tests in Juez et al. [17].

Establishing the link between the flow and sediment transport is crucial in understanding the geomorphological evolution of the lateral embayments. The information related to the accurate quantification of the mass exchange between the main channel and the lateral embayments may be used for the application of measures against sedimentation problems or to identify the magnitude and sources of pollutants, nutrients and carbon, which are fixed to and conveyed with the sediment. For example, the impact of the release of fine sediments by reservoir flushing operations on the in-cavity sedimentation could be better assessed by knowing the interaction between the flow rates and the geometry of lateral embayments. The long-term maintenance of the cavities could thus be guaranteed. Furthermore, as future work the additional

modelling of the sediment particles in suspension will be considered in the LES model to account for their impact on the bulk flow.

5. Conclusions

The main drivers in the mass and momentum exchange between the main channel and symmetrically-distributed river lateral cavity have been identified via large-eddy simulations (LES). Three cases with varying shallowness and flow discharge were analysed for a single embayment geometry. Despite the relatively shallow nature of the flow, the hydrodynamics notably changed for each flow condition, all of which proved to be highly three-dimensional both across the main channel, within the cavities and also in their transition region. In order to elucidate and quantify such complex flow nature, high-resolution LES were carried out to complement the experimental observations so as to understand the driving mechanisms also involved in the sediment transport.

Regarding mass exchange, this study outlines that large streamwise and transversal velocities were mostly found in regions near the bottom and top lids at the mouth of the cavities. A single main vortex occupied most of the volume of each cavity, being the location of its core not uniformly distributed over the water depth. LES captured the dominant Kelvin-Helmholtz flow structures generated and convected over the shear layers developed in the channel-cavity transition. Despite a rigid-lid was adopted to represent the free-surface, LES captured well the standing wave phenomenon originated from pressure field oscillations. This was identified from pressure spectra at various locations across the channel width. Peaks in the spectral energy due to the shear-layer vortices shedding were also observed but only at those locations within or close to the lateral cavities.

The areas of sediment deposition obtained during a previous experimental campaign agreed well with areas of low turbulence and vertical velocities predicted by the LES near the embayments bottom. This study quantified that the gradient of pressure is the main responsible for the transport of transverse momentum out of the cavity, counterbalanced by inwards transport due to convection and Reynolds normal stresses. The identification of the main mechanisms developed in the channel-cavity transition provides new insights into the sediment exchange and deposition processes.

31

References

[1] P. Wood, P. Armitage, Biological effects of fine sediment in the lotic environment, Environmental Management 21 (2) (1997) 203–217, doi: 10.1007/s002679900019.

[2] P. Kemp, D. Sear, A. Collins, P. Naden, I. Jones, The impacts of fine sediment on riverine fish, Hydrological Processes 25 (2011) 1800–1821, doi:10.1002/hyp.7940l.

[3] K. Uno, N. Kazuuma, G. Tsujimoto, T. Kakinoki, Trapping effect of fine sediment in wand, Journal of Japan Society of Civil Engineers, Ser. B3 (Ocean Engineering) 69 (2013) 922–927.

[4] I. Nezu, K. Onitsuka, PIV Measurements of side-cavity open-channel flows. Wando model in rivers, Journal of visualization 5 (2002) 77–84.

[5] J. Ribi, J. Boillat, A. Peter, A. J. Schleiss, Attractiveness of a lateral shelter in a channel as a refuge for juvenile brown trout during hydropeaking, Aquatic Science 76 (2014) 572–541, doi:10.1007/s00027-014-0351-x.

[6] E. Langendoen, C. Kranenburg, R. Booij, Flow patterns and exchange of matter in tidal harbours, Journal of Hydraulic Research 32 (1994) 259–270.

[7] S. A. H. van Schijndel, C. Kranenburg, Reducing the siltation of a river harbour, Journal of Hydraulic Research 36 (1998) 803–814.

[8] M. Thorel, H. Piégay, C. Barthelemy, B. Räpple, C.-R. Gruel, P. Marmonier, T. Winiarski, J.-P. Bedell, F. Arnaud, G. Roux, J. C. Stella, G. Seignemartin, A. Tena-Pagan, V. Wawrzyniak, D. Roux-Michollet,

B. Oursel, S. Fayolle, C. Bertrand, E. Franquet, Socio-environmental implications of process-based restoration strategies in large rivers: should we remove novel ecosystems along the Rhône (France)?, Regional Environmental Change 18 (7) (2018) 2019–2031, ISSN 1436-378X, doi: 10.1007/s10113-018-1325-7.

[9] E. M. Valentine, I. R. Wood, Experiments in longitudinal dispersion with dead zones, Journal of Hydraulic Division 105(HY8) (1979) 999–1016.

[10] W. S. J. Uijttewaal, D. Lehmann, A. van Mazijk, Exchange processes between a river and its groyne fields: Model experiments, Journal of Hydraulic Engineering 127 (11) (2001) 157–172.

[11] V. Weitbrecht, S. A. Socofolosky, G. H. Jirka, Experiments on Mass Exchange between Groin Fields and Main Stream in Rivers, Journal of Hydraulic Engineering 134 (2) (2008) 173–183, doi:10.1061/(ASCE)0733-9429(2008)134:2(173).

[12] L. F. W. Lesack, P. Marsh, River-to-lake connectivities, water renewal, and aquatic habitat diversity in the Mackenzie River Delta, Water Resources Research 46 (12), doi:10.1029/2010WR009607.

[13] A. Sukhodolov, Hydrodynamics of groyne fields in a straight river reach: insight from field experiments, Journal of Hydraulic Research 52(1) (2014) 105–120, doi:10.1080/00221686.2014.880859.

[14] Y. Akutina, Experimental investigation of flow structures in a shallow embayment using 3D-PTV. PhD Thesis., Ph.D. thesis, McGill University, Montréal, 2015.

[15] E. Mignot, W. Cai, J. I. Polanco, C. Escauriaza, N. Riviere, Measurement of mass exchange processes and coefficients in a simplified open-channel lateral cavity connected to a main stream, Environmental Fluid Mechanics 17 (2017) 429–448, doi:10.1007/s10652-016-9495-7.

[16] A. Navas-Montilla, C. Juez, M. Franca, J. Murillo, Depth-averaged unsteady RANS simulation of resonant shallow flows in lateral cavities using augmented WENO-ADER schemes, Journal of Computational Physics 395 (2019) 511–536, doi:10.1016/j.jcp.2019.06.037.

33

[17] C. Juez, I. Buhlmann, G. Maechler, A. J. Schleiss, M. J. Franca, Transport of suspended sediments under the influence of bank macroroughness, Earth Surf. Process. Landforms 43 (2018) 271–284, doi: 10.1002/esp.4243.

[18] C. Juez, M. Thalmann, A. J. Schleiss, M. J. Franca, Morphological resilience to flow fluctuations of fine sediment deposits in bank lateral cavities, Advances in Water Resources 115 (2018) 44–59, doi: 10.1016/j.advwatres.2018.03.004.

[19] T. R. Jackson, R. Haggerty, S. V. Apte, A. Coleman, K. J. Drost, Defining and measuring the mean residence time of lateral surface transient storage zones in small streams, Water Resources Research 48 (10), doi: 10.1029/2012WR012096.

[20] T. R. Jackson, R. Haggerty, S. V. Apte, B. L. O'Connor, A mean residence time relationship for lateral cavities in gravel-bed rivers and streams: Incorporating streambed roughness and cavity shape, Water Resources Research 49 (6) (2013) 3642–3650, doi:10.1002/wrcr.20272.

[21] M. Sanjou, T. Okamoto, I. Nezu, Dissolved oxygen transfer into a square embayment connected to an open-channel flow, International Journal of Heat and Mass Transfer 125 (2018) 1169 – 1180, ISSN 0017-9310, doi: 10.1016/j.ijheatmasstransfer.2018.04.107.

[22] I. Kimura, T. Hosoda, Fundamental properties of flows in open channels with dead zone, Journal of Hydraulic Engineering 123 (2) (1997) 98–107.

[23] V. Nikora, D. Goring, Fluctuations of Suspended Sediment Concentration and Turbulent Sediment Fluxes in an Open-Channel Flow, Journal of Hydraulic Engineering 128 (2) (2002) 214–224.

[24] C. Juez, M. H. Hassan, M. J. Franca, The Origin of Fine Sediment Determines the Observations of Suspended Sediment Fluxes Under Unsteady Flow Conditions, Water Resources Research 54 (2018) 5654–5669, doi: 10.1029/2018WR022982.

[25] A. McCoy, G. Constantinescu, L. J. Weber, Numerical Investigation of Flow Hydrodynamics in a Channel with a Series of Groynes, Journal of Hydraulic Engineering 134 (2) (2008) 157–172, doi: 10.1061/(ASCE)0733-9429.2008134:2.157.

34

[26] G. Constantinescu, A. Sukhodolov, A. McCoy, Mass exchange in a shallow channel flow with a series of groynes: LES study and comparison with laboratory and field experiments, Environmental Fluid Mechanics 9 (2009) 587–615, doi:10.1007/s10652-009-9155-2.

[27] H. Fang, J. Bai, G. He, H. Zhao, Calculations of Nonsubmerged Groin Flow in a Shallow Open Channel by Large-Eddy Simulation, J. Eng. Mech. 140 (2014) 04014016, doi:10.1061/(ASCE)EM.1943-7889.0000711.

[28] W. van Balen, K. Blankaert, W. Uijttewaal, Analysis of the role of turbulence in curved open-channel flow at different water depths by means of experiments, LES and RANS, Journal of Turbulence 11 (12) (2010) 1–34.

[29] C. Juez, J. Murillo, P. García-Navarro, A 2D weakly-coupled and efficient numerical model for transient shallow flow and movable bed, Advances in Water Resources 71 (2014) 93–109, doi:10.1029/2018WR022982.

[30] A. Navas-Montilla, J. Murillo, Asymptotically and exactly energy balanced augmented flux-ADER schemes with application to hyperbolic conservation laws with geometric source terms, Journal of Computational Physics 317 (2016) 108–147, doi:10.1016/j.jcp.2016.04.047.

[31] P. Ouro, B. Fraga, N. Viti, A. Angeloudis, T. Stoesser, C. Gualtieri, Instantaneous transport of a passive scalar in a turbulent separated flow, Environ. Fluid Mech. 18 (2) (2018) 487–513, doi:10.1007/s10652-017-9567-3.

[32] A. McCoy, G. Constantinescu, L. J. Weber, Exchange Processes in a Channel with Two Vertical Emerged Obstructions, Flow, Turbulence and Combustion 77 (2006) 97–126, doi:10.1007/s10494-006-9039-1.

[33] C. Gualtieri, Numerical Simulation of Flow Patterns and Mass Exchange Processes in Dead Zones, in: 4th International Congress on Environmental Modelling and Software, Barcelona, Spain, 2008.

[34] P. Ouro, B. Fraga, U. Lopez-Novoa, T. Stoesser, Scalability of an Eulerian-Lagrangian large-eddy simulation solver with hybrid

MPI/OpenMP parallelisation, Computers & fluids 179 (2019) 123–136, doi:10.1016/j.compfluid.2018.10.013.

[35] Federal Office of Environment, Hydrological Data Service for watercourses and lakes, URL `http://www.bafu.admin.ch/wasser`, 2016.

[36] P. Ouro, T. Stoesser, B. Fraga, U. Lopez-Novoa, Hydro3D repository, doi:10.5281/zenodo.1200187, 2018.

[37] Y. Liu, T. Stoesser, H. Fang, A. Papanicolau, A. Tsakiris, Turbulent flow over an array of boulders placed on a rough permeable bed, Computers and Fluids 158 (2017) 120–132.

[38] P. Ouro, C. A. M. E. Wilson, P. Evans, A. Angeloudis, Large-eddy simulation of shallow turbulent wakes behind a conical island, Phys. Fluids 29 (12) (2017) 126601, ISSN 1070-6631, doi:10.1063/1.5004028.

[39] T. Stoesser, Physically Realistic Roughness Closure Scheme to Simulate Turbulent Channel Flow over Rough Beds within the Framework of LES, J. Hydraul. Eng. 136 (2010) 812–819, doi:10.1061/(ASCE)HY.1943-7900.0000236.

[40] T. Stoesser, C. Braun, M. García-Villalba, W. Rodi, Turbulence Structures in Flow over Two-Dimensional Dunes, J. Hydraul. Eng. 134 (1) (2008) 42–55, ISSN 0733-9429, doi:10.1061/(ASCE)0733-9429(2008)134:1(42).

[41] W. Rodi, G. Constantinescu, T. Stoesser, Large-Eddy Simulation in Hydraulics, CRC Press, ISBN 978-0-203-79757-0, 2013.

[42] S. Bomminayuni, T. Stoesser, Turbulence Statistics in an Open-Channel Flow over a Rough Bed, Journal of Hydraulic Engineering 137 (11) (2011) 1347–1358.

[43] M. Cevheri, R. McSherry, T. Stoesser, A local mesh refinement approach for large-eddy simulations of turbulent flows, International Journal for Numerical Methods in Fluids 82 (2016) 261–285.

[44] F. Nicoud, F. Ducros, Subgrid-scale stress modelling based on the square of the velocity gradient tensor, Flow, turbulence and Combustion 62 (1999) 183–200, doi:10.1023/A:1009995426001.

[45] M. Koken, G. Constanstinescu, An investigation of the dynamics of coherent structures in a turbulent channel flow with a vertical sidewall obstruction, Physics of Fluids 21 (8) (2009) 085104, doi:10.1063/1.3207859.

[46] T. Meile, J.-L. Boillat, A. J. Schleiss, Flow Resistance Caused by Large-Scale Bank Roughness in a Channel, Journal of Hydraulic Engineering 137 (12) (2011) 1588–1597, doi:10.1061/(ASCE)HY.1943-7900.0000469.

[47] B. A. Tuna, E. Tinar, D. Rockwell, Shallow flow past a cavity: globally coupled oscillations as a function of depth, Experiments in Fluids 54 (2013) 1586, doi:10.1007/s00348-013-1586-3.

[48] M. Sanjou, I. Nezu, Hydrodynamic characteristics and related mass-transfer properties in open-channel flows with rectangular embayment zone, Environmental Fluid Mechanics 13 (2013) 527–555, doi: 10.1007/s10652-013-9279-2.

[49] C. J. Kähler, S. Scharnowski, C. Cierpka, On the uncertainty of digital PIV and PTV near walls, Experiments in Fluids 52 (6) (2012) 1641–1656, ISSN 1432-1114, doi:10.1007/s00348-012-1307-3.

[50] E. Mignot, W. Cai, G. Launay, N. Riviere, C. Escauriaza, Coherent turbulent structures at the mixing-interface of a square open-channel lateral cavity, Physics of Fluids 25 (2016) 045104, doi:10.1063/1.4945264.

[51] D. Rockwell, C. Knisely, Observations of the three-dimensional nature of unstable flow past a cavity, Physics of fluids 23 (1980) 425, doi: 10.1063/1.863009.

[52] M. Wölfinger, C. A. Ozen, D. Rockwell, Shallow flow past a cavity: Coupling with a standing gravity wave, Physics of fluids 24 (2012) 104103, doi:10.1063/1.4761829.

[53] V. Nikora, R. Nokes, W. Veale, M. Davidson, G. H. Jirka, Large-scale turbulent structure of uniform shallow free-surface flows, Environmental Fluid Mechanics 7 (2007) 159–172, doi:0.1007/s10652-007-9021-z.

[54] J. Sommeria, Experimental study of the two-dimensional inverse energy cascade in a square box, Journal of Fluid Mechanics 170 (1986) 139–168, doi:10.1017/S0022112086000836.

[55] V. Nikora, Origin of the "21" Spectral Law in Wall-Bounded Turbulence, Physical Review Letters 83 (1999) 734, doi: 10.1103/PhysRevLett.83.734.

[56] R. Kraichnan, Inertial Ranges in Two-Dimensional Turbulence, Physics of Fluids 10 (1967) 1417, doi:10.1017/S0022112086000836.

Declaration of interests

The authors declare that they have no known competing financial interests or personal relationships that could have appeared to influence the work reported in this paper.

Author Contribution

P.O. performed the numerical simulations and contributed to the manuscript; C.J. wrote the introduction and discussion; M.F. helped to conceptualised the research, and contributed to and reviewed the manuscript.